ENVIRONMENTAL RESEARCH
LETTERS

PURPOSE-LED
PUBLISHING™

LETTER • OPEN ACCESS

Tundra recovery post-fire in the Yukon–Kuskokwim Delta, Alaska

To cite this article: Leah K Clayton *et al* 2025 *Environ. Res. Lett.* **20** 044018

ENVIRONMENTAL RESEARCH
LETTERS

CrossMark

OPEN ACCESS

RECEIVED
21 January 2025

REVISED
24 February 2025

ACCEPTED FOR PUBLICATION
12 March 2025

PUBLISHED
25 March 2025

LETTER

Tundra recovery post-fire in the Yukon–Kuskokwim Delta, Alaska

Leah K Clayton[1,*], Kevin Schaefer[2], Elizabeth E Hoy[3,4], Clayton D Elder[5,6], Nancy H F French[7], Gerald V Frost[8], Elizabeth Wig[9] and Xuhui Lee[10]

[1] Department of Earth & Planetary Sciences, Yale University, New Haven, CT, United States of America
[2] National Snow and Ice Data Center, Cooperative Institute for Research in Environmental Sciences, University of Colorado Boulder, Boulder, CO, United States of America
[3] NASA Goddard Space Flight Center, Greenbelt, MD, United States of America
[4] Global Science & Technology, Inc., Greenbelt, MD, United States of America
[5] Jet Propulsion Laboratory, California Institute of Technology, Pasadena, CA, United States of America
[6] NASA Ames Research Center, Earth Sciences Division, Moffett Field, CA, United States of America
[7] Michigan Tech Research Institute, Michigan Technological University, Ann Arbor, MI, United States of America
[8] Alaska Biological Research, Inc., Fairbanks, AK, United States of America
[9] Department of Electrical Engineering, Stanford University, Stanford, CA, United States of America
[10] School of the Environment, Yale University, New Haven, CT, United States of America
[*] Author to whom any correspondence should be addressed.

E-mail: leah.clayton@yale.edu

Keywords: tundra, wildfire, permafrost, volumetric water content, active layer thickness

Supplementary material for this article is available online

Abstract

The extent of wildfires in tundra ecosystems has dramatically increased since the turn of the 21st century due to climate change and the resulting amplified Arctic warming. We simultaneously studied the recovery of vegetation, subsurface soil moisture, and active layer thickness (ALT) post-fire in the permafrost-underlain uplands of the Yukon–Kuskokwim Delta in southwestern Alaska to understand the interaction between these factors and their potential implications. We used a space-for-time substitution methodology with 2017 Landsat 8 imagery and synthetic aperture radar products, along with 2016 field data, to analyze tundra recovery trajectories in areas burned from 1953 to 2017. We found that spectral indices describing vegetation greenness and surface albedo in burned areas approached the unburned baseline within a decade post-fire, but ecological succession takes decades. ALT was higher in burned areas compared to unburned areas initially after the fire but negatively correlated with soil moisture. Soil moisture was significantly higher in burned areas than in unburned areas. Water table depth (WTD) was 10 cm shallower in burned areas, consistent with 10 cm of the surface organic layer burned off during fire. Soil moisture and WTD did not recover in the 46 years covered by this study and appear linked to the long recovery time of the organic layer.

1. Introduction

The Arctic is warming at rates up to four times the global average, resulting in rapid and enduring changes [1–5]. In the treeless tundra biome, fire frequency, intensity, and burned area markedly increased in recent decades, illuminating how tundra fire is changing with anthropogenic climate change [6–11]. Tundra fires have significant implications ranging from local changes in vegetation and biogeochemical cycling to global-scale impacts from greenhouse gas emissions [12–14]. As air temperatures increase, precipitation becomes more variable and extreme, and storms intensify, the dry conditions and lightning events that prime tundra landscapes for fire are likely to become more common [15–17].

Fire causes permafrost—ground that stays at or below 0 °C for two or more consecutive years—to thaw by altering the local thermal and radiative energy balance. Fire decreases the surface albedo and eliminates shading and insulation from organic material [18]. This increases the energy absorbed by the surface, thereby increasing soil temperature and active layer thickness (ALT). ALT—maximum thaw depth reached at the end of the thaw season—is a key indicator of permafrost status [19]. ALT increases due to fire have historically recovered in approximately 25 years as vegetation recovered [20, 21]. However, post-fire permafrost thaw in addition to climate-driven thaw may lead to long-term changes [22–24].

Surface soil moisture increases after a fire, and this has been attributed to decreases in transpiration and precipitation interception while vegetation reestablishes [25–27]. However, while vegetation regrows rapidly within a few years post-burn [18], the increase in soil moisture persists for decades. The reduction of transpiration immediately post-fire alone cannot explain why elevated soil moisture persists.

Post-fire succession can take decades to recover pre-burn communities [3, 28]. For example, lichen mats, which play an insulating role, can take over four decades to near pre-fire cover abundance [3, 29, 30]. Shrubification—an increase in vascular woody plants—is a post-fire response in some areas, as well as a broader phenomenon correlated with warming temperatures [4]. Increased shrub cover may worsen tundra fire by altering the fuel landscape and maintain a warmer soil column by trapping snow and insulating the ground in the winter [3, 14, 31, 32].

A clear picture of tundra landscape recovery after fire is critical to understanding the impact of fire under a changing climate. The Yukon–Kuskokwim Delta (YKD), the warmest tundra region in Alaska, lies in the discontinuous permafrost zone with mean annual average air temperatures near 0 °C [33], making it distinctly vulnerable to permafrost thaw and degradation from fire disturbance [34, 35]. Southwestern Alaska, where the YKD is situated, has experienced a large proportion of global tundra fire activity since 2015 [11, 20] and has a robust burn perimeter record, making it an ideal setting to study tundra fire recovery. Previous studies have used remote sensing data, field studies, and space-for-time substitutions to create statistical models of tundra fire recovery, but each focused only on specific landscape characteristics [3, 20, 25, 36].

Here, we simultaneously study the recovery of vegetation, soil moisture, and ALT to understand the impacts of fire in the YKD. We create statistical models of recovery using space-for-time substitutions with remote sensing data. We analyze indices derived from Landsat 8 data that describe vegetation, albedo, and surface moisture content. We investigate ALT, surface subsidence, soil volumetric water content (VWC), and water table depth (WTD) derived from airborne synthetic aperture radar (SAR) alongside *in situ* data, both from NASA's Arctic-Boreal Vulnerability Experiment (ABoVE). Simultaneously evaluating surface characteristics and subsurface geophysical variables provides a unique, integrated picture of vegetation, hydrology, and permafrost thermodynamics recovery after tundra fire.

2. Methods

2.1. Study area

The YKD is a large tundra region in southwestern Alaska (figure 1) characterized by the deltaic landscapes of the Yukon and Kuskokwim Rivers. Inland portions encompass eolian and volcanic upland environments where soil, fuel, and climatic characteristics are conducive to fire [37]. Unburned tundra vegetation is comprised of lichens, *Sphagnum* moss, and dwarf shrubs [3, 28, 38]. Lichens are a primary fuel for fires, and fire severity is usually moderate to low [3]. Over 8.5 million acres have been recorded as burned from 1950 to 2022 in the YKD, with over half of this area being burned since 2015 [39]. The Yup'ik and Cup'ik peoples inhabiting the YKD compose one of the largest Indigenous populations in the circumpolar Arctic [2], and several of their villages are near fire perimeters in the study area.

The YKD is underlain by ice-rich, discontinuous permafrost with numerous thermokarst lakes. Most of the burn perimeters in the study area are within the Izaviknek-Kingaglia Uplands, where lakes are less common due to the hilly topography. Permafrost is widespread on shallow hillslopes but not in gullies or under streams or lakes [20]. Modeling predicts the region will not be underlain by permafrost by 2100 [34, 35]. Our study area is approximately 85 km northwest of the nearest long-term climatological station at Bethel Airport, where the mean annual average air temperature was −0.3 °C from 1981–2020 [40].

2.2. *In situ* ALT and VWC

In situ ALT and VWC data were collected in August 2016 within and around the extensive 2015 Kuka Creek and Izavlknek River fire perimeters as a part of the NASA ABoVE field campaign [42, 43]. ALT—as reasonably approximated by late-season thaw depth—was measured by pushing a mechanical probe into the ground until the permafrost table was reached (uncertainty ± 3 cm) [42]. Active layer dielectric permittivity was measured using ground penetrating radar [42] and transformed into VWC integrated over the depth of the active layer ($\mathrm{VWC}_{\mathrm{bulk}}$) using a petrophysical transform [44]. Out of the 916 collocated measurements of ALT and $\mathrm{VWC}_{\mathrm{bulk}}$ in the study area, the field team classified 204 as burned and 716 as unburned. One record was removed due to an unrealistic $\mathrm{VWC}_{\mathrm{bulk}}$ value that exceeded 1.00 $\mathrm{cm}^3\ \mathrm{cm}^{-3}$.

2.3. SAR-derived variables

The Permafrost Dynamics Observatory (PDO) dataset is based on airborne SAR flown in 2017 as part of NASA ABoVE [45, 46]. We analyzed rasters of seasonal subsidence (hereafter 'subsidence'), ALT, ALT uncertainty, WTD, and the average VWC integrated over four depths: from the surface to 6 cm depth (VWC_6), to 12 cm (VWC_{12}), to 20 cm (VWC_{20}), and

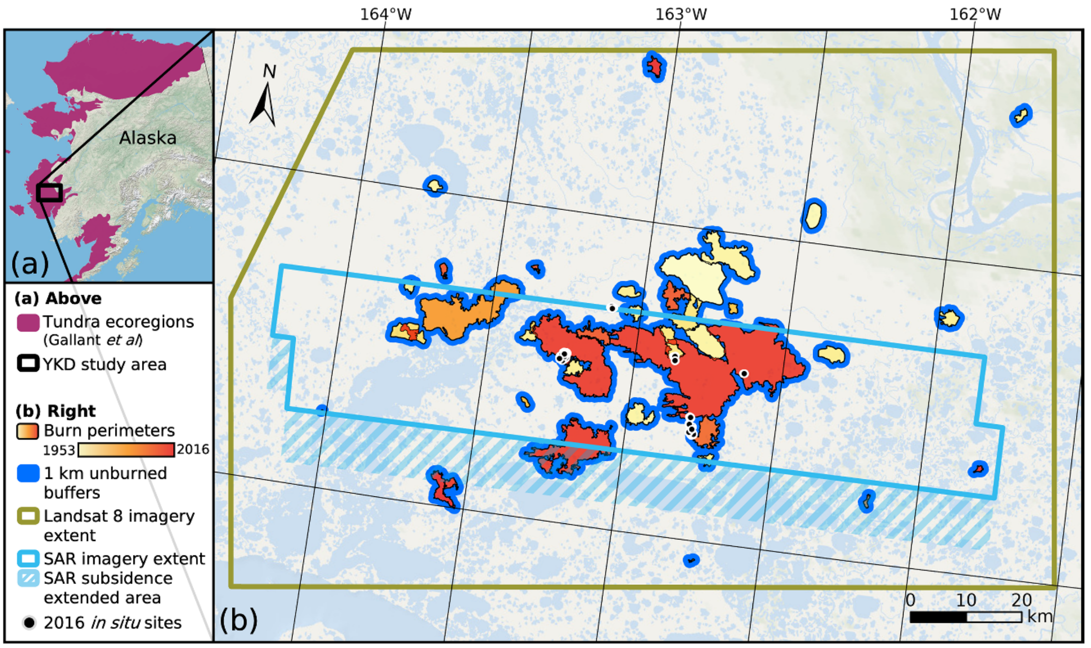

Figure 1. Study area in the Yukon–Kuskokwim Delta (YKD). Panel (a) shows the study area within the state of Alaska and the Alaskan tundra ecoregions as defined by Gallant *et al* [41]. Panel (b) depicts the burn perimeters colored by fire year, the 1 km unburned buffers surrounding each burn perimeter, the extents of the Landsat 8 and airborne synthetic aperture radar (SAR) imagery, and the locations of *in situ* data from August 2016. Seasonal subsidence relies only on L-band SAR and thus extends further south (blue hatching) than the SAR products that use both P- and L-band SAR. Light blue shading in the basemap signifies open water bodies. The upper northeast corner of the scene north of the Yukon River is not classified as tundra [41] and had high cloud cover in the Landsat 8 scene; cloud masking effectively removed the only fire perimeter in the record from this region, the 1972 Engineer Lake Fire.

VWC_{bulk} [47]. The ground surface settles over the thaw season since liquid water takes up less volume than ice, and this subsidence is quantified with L-band interferometric SAR (InSAR). InSAR requires two temporally separate SAR acquisitions within the thaw season, which were acquired on 17 June and 17 September 2017 for the YKD. The retrieval algorithm estimates the remainder of the variables from spatially co-registered L-band and P-band SAR using a physical model that describes the vertical distribution of organic matter, soil porosity, and soil water [20, 47–49]. All variables have a 30 m spatial resolution. The PDO team filtered out atmospheric noise, masked water bodies, and used the *in situ* data described in section 2.2 to validate the products [48].

2.4. Landsat 8 variables

We calculated surficial indices from Landsat Collection-2 Analysis Ready Data surface reflectance [50]. We selected the scene for the space-for-time substitution based on the following criteria: (1) an acquisition date between June and August 2017, (2) coverage of the entire study area on one date, and (3) minimal clouds. Summer timing is contemporaneous with the SAR and corresponds with the maximum available light for remote sensing [18], active layer thaw season, absence of snow, and vegetation growing season. Dense smoke was not a concern since no fires were recorded within the study area during summer 2017 [51]. These criteria resulted in one possible scene acquired by the Landsat 8 Operational Land Imager and Thermal Infrared Sensor (OLI-TIRS) on 5 June. The resulting swath is approximately 150 × 95 km with the native resolution of 30 m. We applied a cloud mask, removing pixels with surface reflectance values >0.09 in the visible blue band (Landsat 8 B2) [52]. We masked all surface water, cloud shadows, and possible snow or ice by removing all pixels with shortwave infrared (SWIR1; Landsat 8 B7) values <0.09. For both masks, we performed iterations to determine the most accurate thresholds. We calculated the indices summarized in table 1: normalized difference vegetation index (NDVI), normalized difference moisture index (NDMI), normalized burn ratio (NBR), tasseled cap transform (TCT brightness, greenness, and wetness), and broadband shortwave surface albedo (hereafter ‘albedo’). Near-infrared (NIR; Landsat 8 B5) was additionally analyzed since it is present in all indices.

2.5. Burn perimeters and classifications

Burn perimeter polygons were obtained by merging records from the Alaska Large Fire Database [60] and Monitoring Trends in Burn Severity [61] database from the start date of each database (1942 [62] and 1984 [63], respectively) through 2017 as described in Yoseph *et al* [64]. Merged records span from 1953 to

Table 1. Surficial indices calculated from Landsat 8 OLI-TIRS surface reflectance bands with equations and citing literature. For Landsat 8, B2 is visible blue wavelengths (0.450–0.51 μm), B3 is visible green (0.53–0.59 μm), B4 is visible red (0.64–0.67 μm), B5 is near infrared (NIR; 0.85–0.88 μm), B6 is shortwave infrared (SWIR1; 1.57–1.65 μm), and B7 is shortwave infrared (SWIR2; 2.11–2.29 μm). Broadband shortwave surface albedo was approximated from the Landsat 8 surface reflectance band ('narrowband') data using the coefficients derived for Landsat 7 [53], updated with the Landsat 8 bands of the corresponding wavelength ranges.

Index	Name	Equation	Citing literature
NDVI	Normalized difference vegetation index	$\mathrm{NDVI} = (B5 - B4)\,/\,(B5 + B4)$	[54]
NDMI	Normalized difference moisture index	$\mathrm{NDMI} = (B5 - B6)\,/\,(B5 + B6)$	[55–57]
NBR	Normalized burn ratio	$\mathrm{NBR} = (B5 - B7)\,/\,(B5 + B7)$	[58]
TCT brightness	Tasseled cap transform brightness	$TCT_{\mathrm{bright}} = (B2 * 0.3029) + (B3 * 0.2786) + (B4 * 0.4733) + (B5 * 0.5599) + (B6 * 0.508) + (B7 * 0.1872)$	[59]
TCT greenness	Tasseled cap transform greenness	$TCT_{\mathrm{green}} = (B2 * -0.2941) + (B3 * -0.243) + (B4 * -0.5424) + (B5 * 0.7276) + (B6 * 0.0713) + (B7 * -0.1608)$	[59]
TCT wetness	Tasseled cap transform wetness	$TCT_{\mathrm{wet}} = (B2 * 0.1511) + (B3 * 0.1973) + (B4 * 0.3283) + (B5 * 0.3407) + (B6 * -0.7117) + (B7 * -0.4559)$	[57, 59]
Albedo	Broadband shortwave surface albedo	α_{short}=$((0.356{*}B2) + (0.130{*}B4) + (0.373{*}B5) + (0.085{*}B6) + (0.072{*}B7) - 0.0018)\,/\,1.016$	[53]

2016 in the YKD since no burns were recorded in 2017 [51].

We defined burned areas as regions that burned once within the record. We defined reburned areas as regions where burn perimeter polygons from separate fire years overlapped, and we analyzed these separately from burned areas. No area in this record was recorded to have burned more than twice. We considered unburned areas as any area that was not recorded to have burned during the time span of the burn perimeter record. We defined a 1 km unburned buffer surrounding each burn perimeter, removing any regions that overlapped with other burn perimeters. We experimented with several buffer widths and selected the 1 km buffer since it yielded a pixel sample size most similar to the number of pixels within the burned polygons without extending so far from the burn perimeter that it sampled a dissimilar landscape. The number of burn perimeters and pixels by fire year is presented in the supplement (tables S1 and S2).

2.6. Burn classification and post-fire trajectory analyses

We performed all analyses throughout in Python [65–67]. We calculated zonal statistics for each variable, fire year, and burn classification. For each variable, we aggregated all fire years by burn classification and tested for statistical significance using analysis of variance (ANOVA) with post-hoc Tukey's honest significant difference (HSD) test with a significance level of $\alpha = 0.05$. Several variables, particularly VWC and WTD, deviate significantly from normal distributions, suggesting that the mean may not best describe the data. However, given that tens to hundreds of thousands of pixels are sampled for each classification, parametric statistics are justified under the Central Limit Theorem [68]. Histograms and non-parametric statistics can be found in the supplement (figures S1 and S2; tables S3 and S4).

By fire year, we tested the significance of the difference between pairs of burned and unburned buffer statistics for each variable at a level of significance of $\alpha = 0.05$. We used Welch's T-tests to test whether the burned area mean was significantly different from the unburned area mean [69]. We performed Mood's median tests to test whether the burned and unburned medians come from populations with the same median [70]. For both tests, a p-value less than 0.05 rejects the null hypothesis and indicates that there is a significant difference between the burned and unburned statistics.

We used a space-for-time substitution to model the post-fire trajectory of remotely-sensed variables over time [20, 36]. A burn perimeter from x years ago represents conditions from x years of post-fire recovery. This tests the assumption that all variations in a variable for a given fire year relative to other fire years can be attributed to time since burn. This analysis implicitly assumes that all burned areas respond identically post-fire; it is only plausible for use in this region because the pre-burn geophysical and ecological conditions are approximately homogenous across the landscape.

We modeled recovery curves for each variable using non-linear least squares curve fits of the time since burn (2017 minus fire year) and Δ (the burned

Table 2. Burned and unburned classification means, standard deviations, and medians for Landsat and SAR variables. All the means and medians for each variable reject the null hypothesis that the burned and unburned statistic are identical (Welch's T-test, Mood's median test; $\alpha = 0.05$). Variables presented without units are dimensionless.

Variable	Class	Mean	Standard deviation	Median
NBR	Burned	0.215	0.153	0.234
	Unburned	0.346	0.068	0.343
NDMI	Burned	−0.043	0.112	−0.029
	Unburned	0.056	0.060	0.051
NDVI	Burned	0.521	0.079	0.531
	unburned	0.561	0.055	0.554
NIR	Burned	0.238	0.054	0.237
	Unburned	0.286	0.033	0.291
Albedo	Burned	0.125	0.021	0.125
	Unburned	0.144	0.017	0.147
TCT greenness	Burned	0.100	0.039	0.101
	Unburned	0.130	0.021	0.130
TCT brightness	Burned	0.354	0.041	0.355
	Unburned	0.386	0.040	0.394
TCT wetness	Burned	−0.125	0.028	−0.127
	Unburned	−0.100	0.021	−0.103
VWC_6 ($cm^3\ cm^{-3}$)	Burned	0.786	0.129	0.847
	Unburned	0.635	0.156	0.626
VWC_{12} ($cm^3\ cm^{-3}$)	burned	0.814	0.114	0.868
	unburned	0.687	0.147	0.689
VWC_{20} ($cm^3\ cm^{-3}$)	Burned	0.789	0.092	0.831
	Unburned	0.691	0.123	0.704
VWC_{bulk} ($cm^3\ cm^{-3}$)	Burned	0.628	0.057	0.628
	Unburned	0.595	0.075	0.589
Subsidence (m)	Burned	0.032	0.006	0.032
	Unburned	0.030	0.005	0.030
ALT (m)	Burned	0.551	0.156	0.543
	Unburned	0.543	0.159	0.535
WTD (m)	Burned	0.157	0.137	0.100
	Unburned	0.258	0.179	0.246

area mean minus the unburned area mean). We determined the most suitable regression by residual plots and the coefficients of determination (R^2) and calculated 95th percentile confidence intervals. If the regression line intersected the x-axis, the 'zero-effect line,' this x–intercept was rounded up to the nearest whole year and termed 'recovery time' [18, 25]. The Landsat 8 scene covered all burn perimeters in the record, so the fire years ranged from 1953 to 2016 (64–1 years since burn). The airborne SAR swaths are smaller, and the earliest burn perimeter in the swaths burned in 1971 (46–1 years since burn).

3. Results

3.1. Burned and unburned classifications

For all variables across both remote sensing data sources, the burned and unburned classifications aggregated over all fire years had significantly different means and medians (table 2). For all Landsat variables, subsidence, and WTD, the burned area means and medians are lower than the corresponding unburned statistics. For all VWC classifications and ALT, the burned area means and medians are higher than the corresponding unburned statistics.

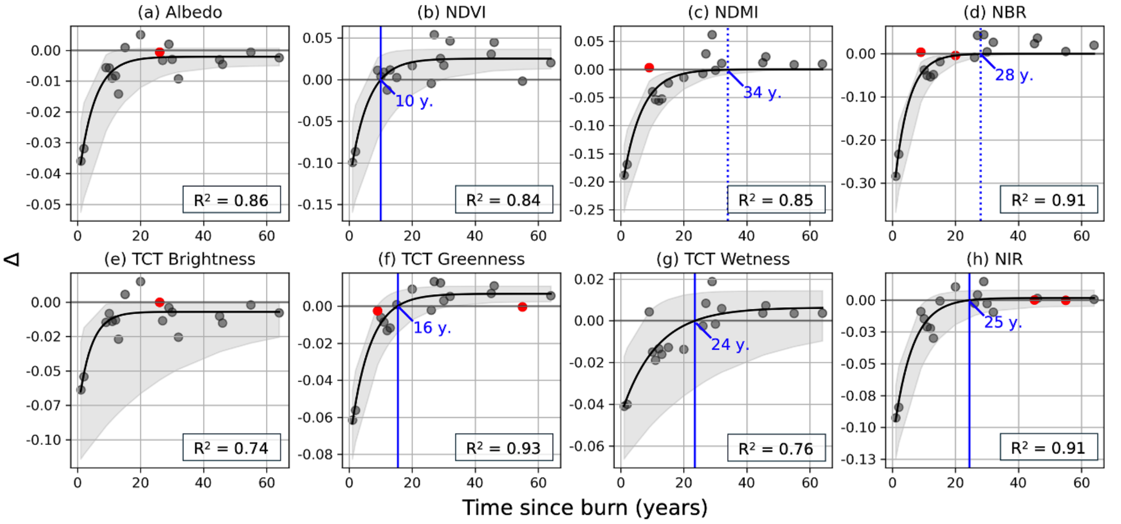

Figure 2. Recovery curves for Landsat 8 variables. Grey points represent the difference (Δ) between the average variable value in the burned area and the average value in the surrounding 1 km unburned buffer for each burn perimeter year; standard error values are small and presented in table S5. Red points indicate years when there is no statistically significant difference between the burned area mean and the 1 km unburned buffer mean when tested with Welch's T-test ($\alpha = 0.05$). The black lines are exponential decay regressions and grey shading indicates 95th percentile confidence intervals; regression equations can be found in table S6. Solid blue vertical lines indicate when a regression intersects the x-axis, or zero-effect line, and this is indicative of recovery. Dotted blue vertical lines indicate where regressions in (c) NDMI and (d) NBR appear to converge with the x-axis due to the regression equation. Albedo (a) and TCT brightness (e) regressions asymptote at $\Delta < 0$.

While an increase in VWC is observed at all depths, it is most pronounced at the surface in VWC_6 and decreases in magnitude as VWC is integrated over more of the active layer to be lowest in VWC_{bulk}.

3.2. Space-for-time substitution recovery curves

All Landsat variables in the burned areas show the greatest deviation from the unburned buffer in the first year post-fire with recovery curves that gradually trend towards zero difference over time (figure 2). All Landsat variables were best fit by exponential decay regressions. NDMI and NBR were fit with exponential decay regressions without a vertical shift parameter to overcome unmitigable overflow errors in Python. NDMI and NBR regressions were forced to approach zero, or 'perfect recovery,' over time, but both were well fit by the model. Coefficient of determination values across variables indicate that 74%–91% of the variation in Δ post-fire can be explained by the time since burn with the exponential decay models.

Indices that quantify similar phenomena—such as vegetation health and density, surface wetness, and surface reflectance and albedo—exhibited similar recovery behavior. NDVI and TCT greenness reached the zero-effect line 10 and 16 years post-fire, respectively (figures 2(b) and (f)). NDMI and TCT wetness, had longer recovery times of 34 and 24 years, respectively (figures 2(c) and (g)). NBR is indistinguishable from the x-axis 28 years since burn (figure 2(d)). NIR crossed the zero-effect line at 25 years since burn (figure 2(h)). Neither model representing surface reflectivity—albedo nor TCT brightness—converged with the zero-effect line (figures 2(a) and (e)). However, the 95th percentile confidence intervals reached the zero-effect line within 15–20 years post-burn, and both regressions asymptote at very small, negative values within two decades. Conversely, NDVI, TCT greenness, TCT wetness, and NIR regressions exceeded the zero-effect line within the 64-year extent.

The SAR-derived variables were fit with linear regressions as the most parsimonious model (figure 3). With the exception of subsidence, all recovery curves showed that burned area means did not recover to unburned levels within 46 years post-burn (figure 3). Subsidence reached the zero-effect line 29 years post-fire, and all Δ values are less than 5 mm. None of the slopes of the regressions were significantly different from zero, and the 95th percentile confidence intervals indicate that negative or positive trends over time are possible for all variables. The coefficients of determination indicate that time since burn explains less than 4.5% of the variability in Δ from the mean.

For all VWC depths of integration and all but two fire years, VWC is higher in the burned areas than unburned buffers (figures 3(a)–(d)). The regressions indicate a return to the zero-effect line over time scales of 110–320 years, but the R^2 values are very low, the slopes are insignificant, and this extrapolates far beyond the study period. The regressions for both ALT and WTD indicate decreases in burned areas relative to unburned and do not recover over the 46 year time period (figures 3 (e) and (f)).

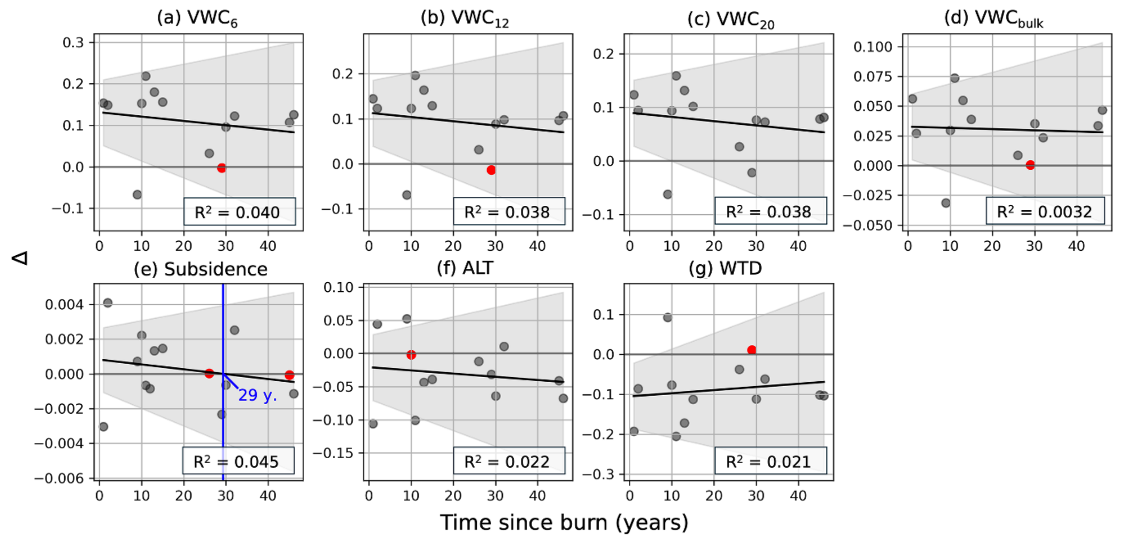

Figure 3. Recovery curves for the SAR-derived variables. Grey points represent the difference (Δ) between the average variable value in the burned area and the average value in the surrounding 1 km unburned buffer for each burn perimeter year; standard error values are small and presented in table S7. All VWC values (a)–(d) are in units of cm^3 cm^{-3}. Subsidence (e), ALT (f), and WTD (g) are in units of m. Red points indicate years when there is no statistically significant difference between the burned area mean and the 1 km unburned buffer mean when tested with Welch's T-test ($\alpha = 0.05$). The black lines are linear regressions and grey shading indicates the 95th percentile confidence intervals. Regression equations are in table S8. Solid blue vertical lines indicate when a regression intersects the x-axis, or zero-effect line, and this is indicative of recovery.

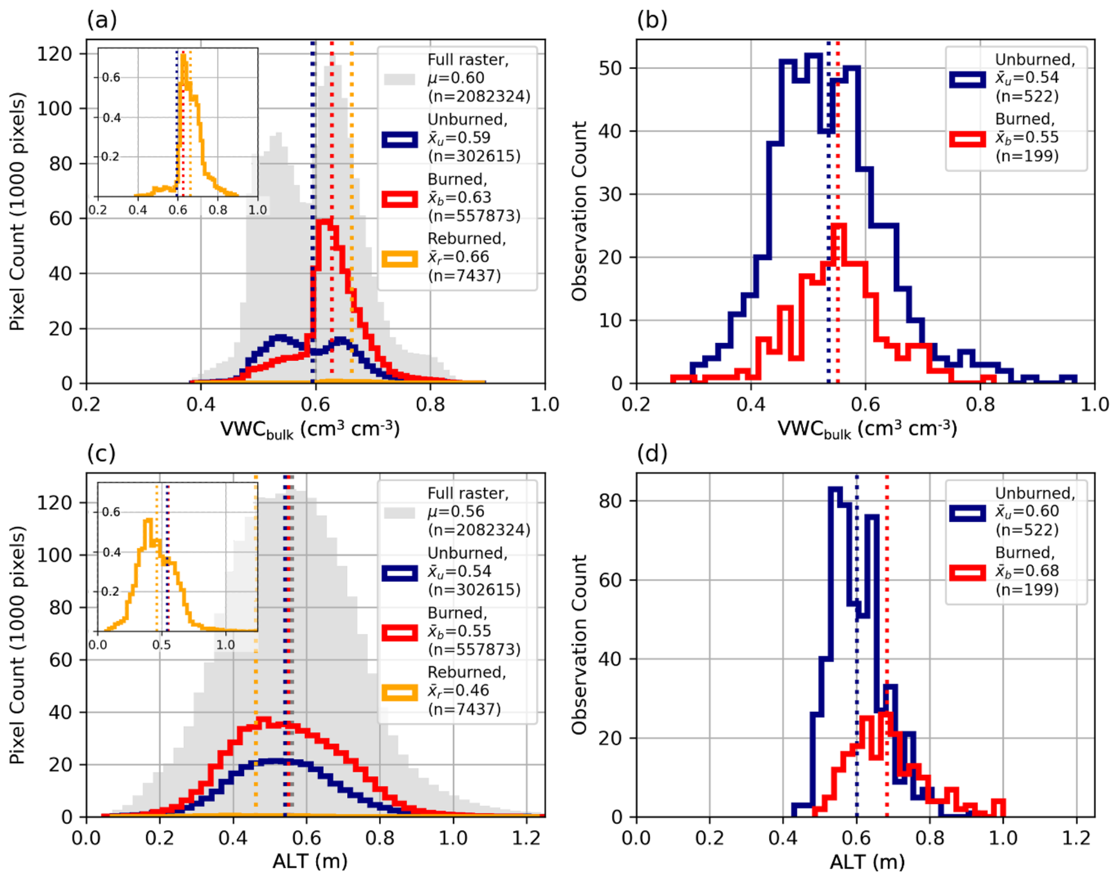

Figure 4. Histograms of VWC$_{bulk}$ and ALT from ((a), (c)) SAR for all fire years and ((b), (d)) *in situ* observational data collected in 2016 in and around 2015 fire perimeters. The first column ((a), (c)) shows burned, unburned buffer, and reburned (expanded in insets due to lower pixel counts) classification distributions relative to the distribution of the entire SAR swath for (a) VWC$_{bulk}$ and (c) ALT. The second column ((b), (d)) depicts the burned and unburned *in situ* (b) VWC$_{bulk}$ and (d) ALT distributions. For all panels, the dotted lines signify the means for each classification listed in the legend, denoted by μ or $\bar{x}$, and all means for all variables are statistically significantly different from each other at $\alpha = 0.05$ by ((a), (c)) ANOVA with post-hoc Tukey's HSD test or ((b), (d)) Welch's t-test.

3.3. Remotely-sensed and *in situ* ALT and VWC

SAR-based VWC_{bulk} shows a bimodal distribution across the entire raster with a lower peak centered around 0.55 cm^3 cm^{-3} and an upper peak at 0.63 cm^3 cm^{-3} (figure 4(a)). The unburned VWC_{bulk} mirrors this bimodal distribution, but the burned and reburned classifications, representing all fire years, have unimodal distributions with the most common VWC_{bulk} values corresponding with the upper peak of the full raster distribution. All SAR-based VWC variables show bimodal distributions across the entire swath and unburned classification but unimodal distributions for the burned and reburned classifications that correspond with the upper peak of the full raster bimodal distribution (figure S2). The *in situ* VWC_{bulk} data indicates a slight bimodality in the unburned distribution, with peaks at approximately 0.47 and 0.57 cm^3 cm^{-3} (figure 4(b)). The burned sample distribution is unimodal with a peak at the mean 0.55 cm^3 cm^{-3}, 0.01 cm^3 cm^{-3} higher than that of the unburned samples.

The SAR-based ALT distribution is unimodal and approximately normal with a mean of 56 cm (figure 4(c)). Mean ALT in burned areas across all fire years is 55 cm, 1 cm higher than that of unburned areas. The mean ALT for reburned areas is 46 cm, lower than all other classifications. The *in situ* burned samples had an average ALT of 68 cm, 8 cm deeper than the unburned average ALT of 60 cm (figure 4(d)).

3.4. Relationship between ALT and VWC_{bulk}

There is a significant negative correlation between VWC_{bulk} and ALT for the burned *in situ* samples, but there is no significant correlation for unburned samples (figure 5). For burned samples, VWC_{bulk} explains nearly 40% of the variation in ALT, with drier active layers correlated with deeper ALT.

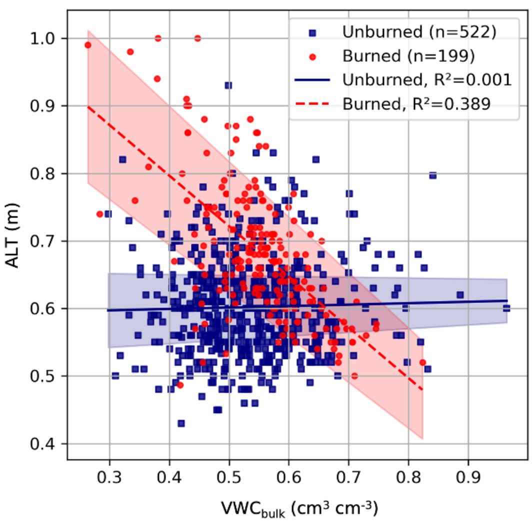

Figure 5. *In situ* VWC_{bulk} and ALT for burned and unburned observations measured in August 2016 in and around 2015 fire perimeters. Linear regression equations are presented in table S9.

4. Discussion

Surficial indices, primarily indicative of vegetation, recovered within 35 years post-fire while VWC, ALT, and WTD did not recover to unburned tundra levels within the 46 year record analyzed. In the *in situ* data, we observed deeper ALT and higher VWC_{bulk} in burned areas than unburned areas and a significant negative relationship between ALT and VWC_{bulk} in burned areas. These results indicate that subsurface geophysical changes due to fire can persist despite apparent spectral recovery on the surface.

The interpretation of these results is, in part, shaped by the space-for-time substitution. The implicit assumptions of homogenous burn severities and pre-burn conditions across fire perimeters are broadly true for the YKD, allowing this analysis to use remote sensing to extend the period studied beyond fieldwork records. However, these models are not time series trajectories of one location sampled over time. Additionally, *in situ* measurements sample the burned and unburned conditions, but they do not represent colocated pre-burn and post-burn pairs of data. Edge effects, including the horizontal transport of water or heat from the burned areas, could affect the proximate unburned buffer regions. However, this was not observed, and the buffer width allows for significant distance from each fire perimeter. These plausible implications from the methods demonstrate the need for repeated data collection over time to understand the pre-burn conditions and post-burn trajectories of tundra, especially as the climate changes. We utilized a combined approach of two remote sensing data sources and *in situ* samples to build a robust picture of tundra recovery post-fire despite these limitations.

4.1. Vegetation succession

Indices indicative of vegetation greenness, health, and density recovered fastest out of all variables studied. NDVI and TCT greenness reached the zero-effect line 10 and 16 years post-fire, respectively. In the YKD, rapid vegetation reestablishment is primarily driven by the resprouting of vascular plants and *Sphagnum* moss that survived the fires [3]. Although vegetation cover is discontinuous for several years post-fire, Frost *et al* found that functional diversity recovered to unburned levels approximately a decade post-fire, corresponding with the greenness results found here [3].

For both NDVI and TCT greenness, the recovery curves significantly exceeded the zero-effect line approximately 30 years post-burn, indicating that vegetation greenness and density are higher in the burned areas than the surrounding buffer after initial recovery. Two potential causes are nutrient availability and vegetation community shift. Increased ALT, elevated nutrient availability, and warmer soil temperatures post-fire can promote vegetation growth beyond that in the unburned condition [13]. Over time, this effect would diminish as the active layer recovers and nutrients are consumed, resulting in a return to the zero-effect line, although the exponential decay models used here prevent this curve shape. Second, community shifts, particularly shrubification and a reduction in lichen cover, can occur post-fire [3, 31, 71]. Frost *et al* found that while shrub cover increased post-fire, this primarily reflected resprouting of existing shrubs; recruitment opportunity was relatively low since the peat in the YKD remained intact during the fire [3]. Anderson *et al* found a significant increase in shrub cover in 2015 burns relative to historic burns in the YKD [28].

A variable lag time in the recovery of other surficial indices demonstrates important ecological feedbacks that result from successional processes. Vegetation and surface wetness indices, NDMI and TCT wetness, reached the zero-effect line at 34 and 24 years, respectively. Neither model for surface albedo nor TCT brightness converged with the zero-effect line, but both recovery curves asymptote at very small, negative values within two decades. Frost *et al* note that lichens, the predominant fire fuel in the YKD, take nearly four decades to reestablish [3]. Vegetation regrowth is rapid, but the plant community composition does not appear to return to pre-fire levels for many decades.

Additionally, our models of greenness recovery may underestimate the recovery time of these indices due to the imagery acquisition date. The Landsat 8 scene was acquired in early June, when the active layer remains mostly frozen and before vegetation phytomass has approached its midsummer peak. As a result, the burned area greenness would exceed the unburned buffer area earlier than vegetation community recovery since vascular plant functional types—particularly graminoids and deciduous shrubs—compose a larger proportion of the live cover in post-fire communities than in unburned, lichen-dominated tundra.

Conversely, fires often terminate at gullies or the edges of surface water, both areas of higher moisture with more vegetation. As such, the 1 km buffer zones may disproportionately represent high NDVI, NDMI, TCT greenness, and TCT wetness. This would set the threshold for 'recovery' higher than the initial pre-burn conditions and could result in artificially long recovery times. The effect of this is likely minimal because the 1 km buffers excluded water bodies and sampled large quantities of pixels beyond the small-scale features. The balance of these phenomena is indicated by recovery times that match others presented in literature, but it is important to accurately quantify these timescales since vegetation communities have broad impacts on permafrost thermodynamics, hydrology, biogeochemistry, and ecosystem services.

4.2. ALT

In situ observations indicate an 8 ± 3 cm deeper ALT one year post-burn relative to unburned tundra. For SAR-based ALT, the burned area ALT is 1 cm deeper on average across all fire years than unburned areas (55 ± 16 cm and 54 ± 16 cm, respectively), and ALT is shallower in burned areas than the unburned buffer for most fire years. ALT uncertainty for the SAR-based ALT is higher in burned areas (29 cm) than for unburned areas (26 cm; figure S3). The high SAR-based ALT uncertainty, especially immediately post-burn, could obscure changes in ALT of the magnitude observed in the *in situ* data. In the YKD, Michaelides *et al* found using a space-for-time substitution with satellite SAR that ALT increased post-burn to a maximum of 26 cm and returned to the background level approximately 25 years post-fire as vegetation recovered [20]. Modeled seasonal subsidence in the space-for-time substitution presented here reached the zero-effect line 29 years post-fire which approximates the timeline of Michaelides *et al*, but the modeled regression is not statistically significant and indicates that time since burn explains less than 5% of the variation in Δ for seasonal subsidence.

It seems likely that the SAR-based recovery curve for ALT presented here does not adequately characterize ALT recovery over time, and, in part, this may be due to vegetation not being explicitly accounted for in the SAR joint retrieval despite representing the top of the soil column [72]. Removing 10 cm of the organic layer from the surface of the soil column while maintaining an active layer of the same thickness would result in 10 cm of newly thawed permafrost (figure 6). Moubarak *et al* found the average burn depth in 2015 fire perimeters in the YKD to be 10 cm [14], which corresponds with our field observations (figure S4). Over time as vegetation grows back and surface albedo recovers, and organic matter reaccumulates and provides insulation, ALT may decrease at a similar rate, resulting in the approximately constant ALT trajectory over time when calculated from SAR, although it seems likely that the high ALT uncertainty could obscure these dynamics.

In burned areas, *in situ* ALT was negatively correlated with VWC_{bulk}, indicating that wetter active layers are correlated with shallower ALT, and average VWC_{bulk} was higher in burned areas. This correlation has previously been attributed to the high latent heat of fusion of water [42]. However, the unburned *in situ* samples show no significant trend between VWC_{bulk} and ALT. This suggests that ALT is more sensitive to VWC_{bulk} in burned areas than in unburned areas, and higher soil moisture may moderate post-fire energy balance effects, such as lower albedo due, to the high latent heat of fusion of water, thereby maintaining shallower active layers [42]. Drier active layers in burned areas are observed to be deeper, and this correlation should be investigated further to understand whether increased ALT post-fire is causing regional drainage and thus a decrease in soil moisture or a decrease in soil moisture is reducing the energy required to freeze and thaw the active layer and thus resulting in deeper thaw depths.

4.3. Soil moisture

VWC was higher and WTD was shallower in the burn perimeters, and neither recovered in the 46-year study period. This effect is most pronounced in near-surface VWC. The WTD moved closer to the surface by an average of 10 cm post-fire and did not return to the zero-effect line over the study period. While previous work has documented increased soil moisture post-fire in the tundra [73], the mechanism is generally attributed to a decrease in transpiration due to vegetation loss in the fires, as in the boreal forest [27, 74]. However, significant transpiring vegetation appears to recover to, or even exceed, the pre-burned level on timescales less than two decades.

Again, interpretation of these results depends, in part, on the SAR joint retrieval methodology [72]. The retrieval algorithm uses the same soil porosity profile for all pixels, which may introduce bias when comparing burned and unburned areas. However, the impact of a fixed porosity curve appears minimal because the estimated VWC agrees with *in situ* data within uncertainty. The estimated WTD represents the most uncertain of the estimated subsurface parameters with few validation data points. Overall, the PDO product still represents high-quality geophysical observations that can be analyzed despite fire history.

We propose that the increase in VWC at shallow depths and decrease in WTD results from the burn depth in the organic layer. An average burn depth of 10 cm corresponds with the 10 cm difference between burned and unburned WTD in this study (figure 6). Burn depth encompasses the loss of surface lichens, moss, and peat. It is not uniform and is highly dependent on the surface vegetation. *Sphagnum*, for example, generally remained intact in the 2015 fires due to its water holding capacity. Lichens, on the other hand, have been a primary fuel for fires in the YKD and are observed to be reduced significantly post-fire and recover slowly over decades [3, 29, 30].

We hypothesize that the slow reestablishment of lichens, and the even slower accumulation of peat, contributes to the persistence of the shallower WTD and higher VWC. These changes in the surface vegetation and organic soil alter VWC since they drive water holding capacity in the upper soil column. The organic layer—comprised of a gradient from live vegetation to organic soil—has a higher porosity than the mineral soil it overlays (figure 6). When the fire burns off the lichen, other vegetation, and some peat, this reduces the water holding capacity of the top layer such that the lower porosity substrates beneath become more readily saturated, assuming the same amount of applied water [73]. While an increase in VWC is observed at all depths, it is most pronounced in VWC_{6}, when the top 6 cm are depth-integrated, and smallest in $\mathrm{VWC}_{\mathrm{bulk}}$. Wig *et al* also observed this effect when analyzing all of PDO flight lines across Alaska and Canada [75].

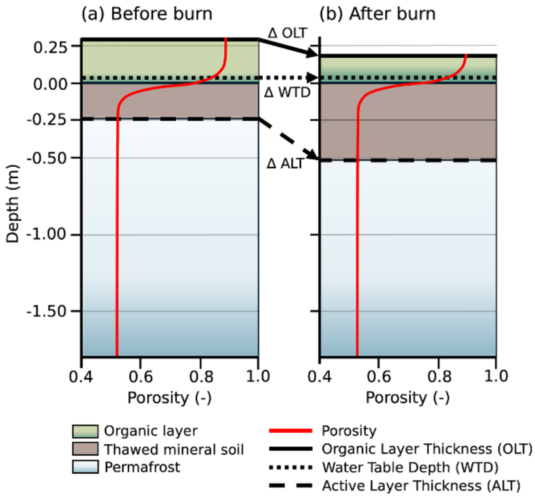

Figure 6. Theoretical porosity profile of soil column before burn (a) and recently post-burn (b) late in the thaw season when the active layer has reached the maximum thaw depth. After the burn, the organic layer thickness (OLT) decreased by 10 cm (figure S4 and [14]), the water table depth (WTD) decreased by 10 cm (this study), and active layer thickness (ALT) increased by 26 cm [20].

Depending on the magnitude of the environmental change, when coupled with long recovery timelines and increased VWC post-fire, there is the possibility of state changes in one or more ecosystem components such as the vegetation community, underlying permafrost, or fire regime. While $\mathrm{VWC}_{\mathrm{bulk}}$ negatively correlates with ALT, high near-surface water saturation increases the thermal conductivity of the top of the soil column, conducting heat more easily from the atmosphere [42]. The highest methane emissions in the YKD were observed in burned areas, especially where burns terminated at water bodies where the water table is nearest the surface [64, 76]. Higher near-surface VWC and a shallower WTD influence vegetation, ALT, energy balance, and carbon cycling.

5. Conclusions

Our analysis indicates that the long-term increase in VWC post-fire results from shallower WTD due to the reduction of the organic layer thickness and resulting changes in the porosity profile. VWC was higher in burned areas than unburned areas and remained so for the 46 years represented by the study. Elevated VWC is most pronounced in the shallower VWC products, indicating that the largest magnitude changes in soil moisture occurred near the surface. WTD appeared 10 cm closer to the surface in burned areas, corresponding to the recorded average burn depth of 10 cm for the 2015 fires in the YKD. *In situ* ALT is negatively correlated with VWC_{bulk}, suggesting that ALT is more sensitive to soil moisture in burned areas than unburned areas, and higher soil moisture may moderate the energy balance effects of lower post-fire albedo. The SAR-based ALT derived using the space-for-time substitution did not show a significant post-fire trend, and we suggest that the recovery dynamics described by previous literature and observations were obscured by the joint retrieval methodology. Vegetation greenness recovers in little more than a decade, indicating that changes in transpiration alone cannot sustain the higher VWC. Surficial spectral recovery of over 30 years indicates the importance of ecological feedbacks associated with successional processes. While some surficial indices recover rapidly, vegetation communities, VWC, and WTD do not recover within the 46 year study period and appear linked to the long recovery time of the organic layer and lichen, as well as the potential for shrubification.

Data availability statement

The data that support the findings of this study are openly available at the following URLs/DOIs: https://doi.org/10.3334/ORNLDAAC/1903; https://doi.org/10.3334/ORNLDAAC/2004; https://doi.org/10.5066/P960F8OC; www.frames.gov/catalog/10465; www.mtbs.gov/.

Acknowledgments

This paper is a contribution of the National Aeronautics and Space Administration (NASA) Arctic-Boreal Vulnerability Experiment (ABoVE). L K C was supported by the Karen L Von Damm '77 Research Fellowship from the Department of Earth and Planetary Sciences at Yale University. E W and K S were supported by NASA ABoVE Grant NNX17AC59A. G V F was supported by NASA ABoVE Grant 80NSSC22K1256. Thank you to the two anonymous reviewers whose comments greatly improved this manuscript.

ORCID iDs

Leah K Clayton https://orcid.org/0000-0002-7493-8101
Kevin Schaefer https://orcid.org/0000-0002-5444-9917
Elizabeth E Hoy https://orcid.org/0000-0002-0104-5118
Clayton D Elder https://orcid.org/0000-0001-9831-2106
Nancy H F French https://orcid.org/0000-0002-2389-3003
Gerald V Frost https://orcid.org/0000-0002-5134-0334
Elizabeth Wig https://orcid.org/0000-0002-8604-0155
Xuhui Lee https://orcid.org/0000-0003-1350-4446

References

[1] Terenzi J, Jorgenson M T and Ely C R 2014 Storm-surge flooding on the Yukon-Kuskokwim Delta, Alaska *Arctic* **67** 360–74
[2] Fienup-riordan A, Frost G V, Nayamin-kelly R, Bhatt U S, Hendricks A S, John M and Odom P 2021 Alaska's changing YK Delta: knowledge exchange between elders and geoscientists, 2018 (ORNL DAAC) (https://doi.org/10.3334/ORNLDAAC/1894)
[3] Frost G V, Loehman R A, Saperstein L B, Macander M J, Nelson P R, Paradis D P and Natali S M 2020 Multi-decadal patterns of vegetation succession after tundra fire on the Yukon-Kuskokwim Delta, Alaska *Environ. Res. Lett.* **15** 025003
[4] Mekonnen Z A *et al* 2021 Arctic tundra shrubification: a review of mechanisms and impacts on ecosystem carbon balance *Environ. Res. Lett.* **16** 053001
[5] Rantanen M, Karpechko A Y, Lipponen A, Nordling K, Hyvärinen O, Ruosteenoja K, Vihma T and Laaksonen A 2022 The Arctic has warmed nearly four times faster than the globe since 1979 *Commun. Earth Environ.* **3** 1–10
[6] French N H F, Jenkins L K, Loboda T V, Flannigan M, Jandt R, Bourgeau-Chavez L L and Whitley M 2015 Fire in arctic tundra of Alaska: past fire activity, future fire potential, and significance for land management and ecology *Int. J. Wildland Fire* **24** 1045–61
[7] Masrur A, Petrov A N and DeGroote J 2018 Circumpolar spatio-temporal patterns and contributing climatic factors of wildfire activity in the Arctic tundra from 2001–2015 *Environ. Res. Lett.* **13** 014019
[8] Masrur A, Taylor A, Harris L, Barnes J and Petrov A 2022 Topography, climate and fire history regulate wildfire activity in the Alaskan tundra *J. Geophys. Res.* **127** e2021JG006608
[9] Higuera P E, Chipman M L, Barnes J L, Urban M A and Hu F S 2011 Variability of tundra fire regimes in Arctic Alaska: millennial-scale patterns and ecological implications *Ecol. Appl.* **21** 3211–26
[10] Chipman M L, Hudspith V, Higuera P E, Duffy P A, Kelly R, Oswald W W and Hu F S 2015 Spatiotemporal patterns of tundra fires: late-quaternary charcoal records from Alaska *Biogeosciences* **12** 4017–27
[11] Sae-Lim J, Russell J M, Vachula R S, Holmes R M, Mann P J, Schade J D and Natali S M 2019 Temperature-controlled tundra fire severity and frequency during the last millennium in the Yukon-Kuskokwim Delta, Alaska *Holocene* **29** 1223–33
[12] Abbott B W *et al* 2021 Tundra wildfire triggers sustained lateral nutrient loss in Alaskan Arctic *Glob. Change Biol.* **27** 1408–30
[13] Heijmans M M P D *et al* 2022 Tundra vegetation change and impacts on permafrost *Nat. Rev. Earth Environ.* **3** 68–84
[14] Moubarak M, Sistla S, Potter S, Natali S M and Rogers B M 2023 Carbon emissions and radiative forcings from tundra wildfires in the Yukon–Kuskokwim River Delta, Alaska *Biogeosciences* **20** 1537–57

[15] Box J E *et al* 2019 Key indicators of Arctic climate change: 1971–2017 *Environ. Res. Lett.* **14** 045010

[16] He J and Loboda T V 2020 Modeling cloud-to-ground lightning probability in Alaskan tundra through the integration of weather research and forecast (WRF) model and machine learning method *Environ. Res. Lett.* **15** 115009

[17] Chen Y, Romps D M, Seeley J T, Veraverbeke S, Riley W J, Mekonnen Z A and Randerson J T 2021 Future increases in Arctic lightning and fire risk for permafrost carbon *Nat. Clim. Change* **11** 404–10

[18] French N H F, Whitley M A and Jenkins L K 2016 Fire disturbance effects on land surface albedo in Alaskan tundra *J. Geophys. Res.* **121** 841–54

[19] World Meteorological Organization (WMO) 2023 Measurement of cryospheric variables *Guide Instruments Methods Observation* vol 2, 2023 edn (WMO) p 105

[20] Michaelides R J, Schaefer K, Zebker H A, Parsekian A, Liu L, Chen J, Natali S, Ludwig S and Schaefer S R 2019 Inference of the impact of wildfire on permafrost and active layer thickness in a discontinuous permafrost region using the remotely sensed active layer thickness (ReSALT) algorithm *Environ. Res. Lett.* **14** 035007

[21] Jones B M, Kanevskiy M Z, Shur Y, Gaglioti B V, Jorgenson M T, Ward Jones M K, Veremeeva A, Miller E A and Jandt R 2024 Post-fire stabilization of thaw-affected permafrost terrain in northern Alaska *Sci. Rep.* **14** 8499

[22] Iwahana G, Uchida M, Liu L, Gong W, Meyer F J, Guritz R, Yamanokuchi T and Hinzman L 2016 InSAR detection and field evidence for thermokarst after a tundra wildfire, using ALOS-PALSAR *Remote Sens.* **8** 218

[23] Rey D M, Walvoord M A, Minsley B J, Ebel B A, Voss C I and Singha K 2020 Wildfire-initiated talik development exceeds current thaw projections: observations and models from Alaska's continuous permafrost zone *Geophys. Res. Lett.* **47** e2020GL087565

[24] Chen Y, Lara M J, Jones B M, Frost G V and Hu F S 2021 Thermokarst acceleration in Arctic tundra driven by climate change and fire disturbance *One Earth* **4** 1718–29

[25] Jenkins L K, Bourgeau-Chavez L L, French N H F, Loboda T V and Thelen B J 2014 Development of methods for detection and monitoring of fire disturbance in the Alaskan tundra using a two-decade long record of synthetic aperture radar satellite images *Remote Sens.* **6** 6347–64

[26] Holloway J E, Lewkowicz A G, Douglas T A, Li X, Turetsky M R, Baltzer J L and Jin H 2020 Impact of wildfire on permafrost landscapes: a review of recent advances and future prospects *Permafr. Periglac Process.* **31** 371–82

[27] Williams M, Zhang Y, Estop-Aragonés C, Fisher J P, Xenakis G, Charman D J, Hartley I P, Murton J B and Phoenix G K 2020 Boreal permafrost thaw amplified by fire disturbance and precipitation increases *Environ. Res. Lett.* **15** 114050

[28] Anderson D P, Michaelides R J, Chen W, Frost G V, Macander M J and Lara M J 2024 Tundra fires and surface subsidence increase spectral diversity on the Yukon–Kuskokwim Delta, Alaska *Environ. Res. Ecol.* **3** 045006

[29] Racine C, Jandt R, Meyers C and Dennis J 2004 Tundra fire and vegetation change along a hillslope on the Seward Peninsula, Alaska, U.S.A *Arct. Antarct. Alp. Res.* **36** 1–10

[30] Jandt R, Joly K, Randy Meyers C and Racine C 2008 Slow recovery of lichen on burned caribou winter range in Alaska Tundra: potential influences of climate warming and other disturbance factors *Arct. Antarct. Alp. Res.* **40** 89–95

[31] Jones B M, Breen A L, Gaglioti B V, Mann D H, Rocha A V, Grosse G, Arp C D, Kunz M L and Walker D A 2013 Identification of unrecognized tundra fire events on the north slope of Alaska *J. Geophys. Res.* **118** 1334–44

[32] Aartsma P, Asplund J, Odland A, Reinhardt S and Renssen H 2021 Microclimatic comparison of lichen heaths and shrubs: shrubification generates atmospheric heating but subsurface cooling during the growing season *Biogeosciences* **18** 1577–99

[33] Miner K R, Turetsky M R, Malina E, Bartsch A, Tamminen J, McGuire A D, Fix A, Sweeney C, Elder C D and Miller C E 2022 Permafrost carbon emissions in a changing Arctic *Nat. Rev. Earth Environ.* **3** 55–67

[34] Jafarov E E, Marchenko S S and Romanovsky V E 2012 Numerical modeling of permafrost dynamics in Alaska using a high spatial resolution dataset *Cryosphere* **6** 613–24

[35] Pastick N J, Jorgenson M T, Wylie B K, Nield S J, Johnson K D and Finley A O 2015 Distribution of near-surface permafrost in Alaska: estimates of present and future conditions *Remote Sens. Environ.* **168** 301–15

[36] Rocha A V, Loranty M M, Higuera P E, Mack M C, Hu F S, Jones B M, Breen A L, Rastetter E B, Goetz S J and Shaver G R 2012 The footprint of Alaskan tundra fires during the past half-century: implications for surface properties and radiative forcing *Environ. Res. Lett.* **7** 044039

[37] Jorgenson M T and Roth J E 2010 Landscape classification and mapping for the Yukon-Kuskokwim Delta, Alaska (ABR, Inc.—Environmental Research & Services) (available at: https://www.academia.edu/106336923/LANDSCAPE_CLASSIFICATION_AND_MAPPING_FOR_THE_YUKON_KUSKOKWIM_DELTA_ALASKA)

[38] He J, Loboda T V, Jenkins L and Chen D 2019 Mapping fractional cover of major fuel type components across Alaskan tundra *Remote Sens. Environ.* **232** 111324

[39] Thoman R 2022 Alaska wildfire season focus on Southwest Alaska *ACCAP Wildfire Webinar 2022* (available at: https://uaf-accap.org/wp-content/uploads/2022/11/2022_ACCAP_SW_Fire_Thoman.pdf)

[40] National Oceanic and Atmospheric Administration National Centers for Environmental Information (NOAA NCEI) 2024 (available at: https://www.ncei.noaa.gov/access/us-climate-normals/)

[41] Gallant A L, Binnian E F, Omernik J M and Shasby M B 1995 *Ecoregions of Alaska [Professional Paper]* Report No.: 1567 (U.S. Geological Survey) (https://doi.org/10.3133/pp1567)

[42] Clayton L K *et al* 2021 Active layer thickness as a function of soil water content *Environ. Res. Lett.* **16** 055028

[43] Schaefer K *et al* 2021 ABoVE: soil moisture and active layer thickness in Alaska and NWT, Canada, 2008–2020 (ORNL Distributed Active Archive Center) (https://doi.org/10.3334/ORNLDAAC/1903)

[44] Engstrom R, Hope A, Kwon H, Stow D and Zamolodchikov D 2005 Spatial distribution of near surface soil moisture and its relationship to microtopography in the Alaskan Arctic coastal plain *Hydrol. Res.* **36** 219–34

[45] Miller C E *et al* 2019 An overview of ABoVE airborne campaign data acquisitions and science opportunities *Environ. Res. Lett.* **14** 080201

[46] Miller C E *et al* 2024 The ABoVE L-band and P-band airborne synthetic aperture radar surveys *Earth Syst. Sci. Data* **16** 2605–24

[47] Chen R H, Michaelides R J, Chen J, Chen A C, Clayton L K, Bakian-Dogaheh K and Zhao Y 2022 ABoVE: active layer thickness from airborne L- and P- band SAR, Alaska, 2017, Ver. 3 (ORNL Distributed Active Archive Center) (https://doi.org/10.3334/ORNLDAAC/2004)

[48] Michaelides R J, Chen R H, Zhao Y, Schaefer K, Parsekian A D, Sullivan T and Chen J 2021 Permafrost Dynamics Observatory—Part I: postprocessing and calibration methods of UAVSAR L-band InSAR data for seasonal subsidence estimation *Earth Space Sci.* **8** e2020EA001630

[49] Parsekian A D, Chen R H, Michaelides R J, Sullivan T D, Clayton L K, Huang L, Zhao Y, Wig E, Moghaddam M, Zebker H and Schaefer K 2021 Validation of permafrost active layer estimates from airborne SAR observations *Remote Sens.* **13** 2876

[50] Earth Resources Observation and Science (EROS) Center 2021 Landsat 4–9 U.S. Analysis ready data, collection 2 (U.S. Geological Survey) (https://doi.org/10.5066/P960F8OC)

[51] Alaska Interagency Coordination Center (AICC) 2024 Alaska fires (available at: https://fire.ak.blm.gov/incinfo/aklgfire.php)

[52] Loboda T V, French N H F, Hight-Harf C, Jenkins L and Miller M E 2013 Mapping fire extent and burn severity in Alaskan tussock tundra: an analysis of the spectral response of tundra vegetation to wildland fire *Remote Sens. Environ.* **134** 194–209

[53] Liang S 2001 Narrowband to broadband conversions of land surface albedo I: algorithms *Remote Sens. Environ.* **76** 213–38

[54] Tucker C J 1979 Red and photographic infrared linear combinations for monitoring vegetation *Remote Sens. Environ.* **8** 127–50

[55] Hardisky M, Klemas V and Smart R 1983 The influence of soil salinity, growth form, and leaf moisture on the spectral radiance of spartina alterniflora canopies *Photogramm. Eng. Remote Sens.* **49** 77–83

[56] Wilson E H and Sader S A 2002 Detection of forest harvest type using multiple dates of Landsat TM imagery *Remote Sens. Environ.* **80** 385–96

[57] Jin S and Sader S A 2005 Comparison of time series tasseled cap wetness and the normalized difference moisture index in detecting forest disturbances *Remote Sens. Environ.* **94** 364–72

[58] López García M J and Caselles V 1991 Mapping burns and natural reforestation using thematic mapper data *Geocarto Int.* **6** 31–37

[59] Baig M H A, Zhang L, Shuai T and Tong Q 2014 Derivation of a tasselled cap transformation based on Landsat 8 at-satellite reflectance *Remote Sens. Lett.* **5** 423–31

[60] Hroback J L, Schmunk G and Lynch M 2024 Alaska large fire database (Fire Research and Management Exchange System (FRAMES)) (available at: https://www.frames.gov/catalog/10465)

[61] MTBS Data Access 2024 Monitoring Trends in Burn Severity (available at: https://mtbs.gov/)

[62] Kasischke E S, Williams D and Barry D 2002 Analysis of the patterns of large fires in the boreal forest region of Alaska *Int. J. Wildland Fire* **11** 131–44

[63] Eidenshink J, Schwind B, Brewer K, Zhu Z-L, Quayle B and Howard S 2007 A project for monitoring trends in burn severity *Fire Ecol.* **3** 3–21

[64] Yoseph E, Hoy E, Elder C D, Ludwig S M, Thompson D R and Miller C E 2023 Tundra fire increases the likelihood of methane hotspot formation in the Yukon–Kuskokwim Delta, Alaska, USA *Environ. Res. Lett.* **18** 104042

[65] Gilles S (others) 2023 Rasterio: geospatial raster I/O for Python programmers MapBox (available at: https://github.com/rasterio/rasterio)

[66] Virtanen P *et al* 2020 SciPy 1.0: fundamental algorithms for scientific computing in Python *Nat. Methods* **17** 261–72

[67] Van den Bossche J *et al* 2023 Geopandas *Zenodo* (https://doi.org/10.5281/zenodo.8009629)

[68] Lumley T, Diehr P, Emerson S and Chen L 2002 The importance of the normality assumption in large public health data sets *Annu. Rev. Public Health* **23** 151–69

[69] Welch B L 1947 The generalization of "student's" problem when several different population varlances are involved *Biometrika* **34** 28–35

[70] Mood A M 1950 *Introduction to the Theory of Statistics* (McGraw-Hill)

[71] Erlandsson R, Arneberg M K, Tømmervik H, Finne E A, Nilsen L and Bjerke J W 2023 Feasibility of active handheld NDVI sensors for monitoring lichen ground cover *Fungal Ecol.* **63** 101233

[72] Chen R H, Michaelides R J, Zhao Y, Huang L, Wig E, Sullivan T D and Schaefer K M 2023 Permafrost Dynamics Observatory (PDO): 2. Joint retrieval of permafrost active layer thickness and soil moisture from L-band InSAR and P-band PolSAR *Earth Space Sci.* **10** e2022EA002453

[73] He J, Chen D, Jenkins L and Loboda T V 2021 Impacts of wildfire and landscape factors on organic soil properties in Arctic tussock tundra *Environ. Res. Lett.* **16** 085004

[74] Bond-Lamberty B, Peckham S D, Gower S T and Ewers B E 2009 Effects of fire on regional evapotranspiration in the central Canadian boreal forest *Glob. Change Biol.* **15** 1242–54

[75] Wig E *et al* 2025 Permafrost Dynamics Observatory: 3. remote sensing big data for the active layer, soil moisture, and greening and browning *Earth Space Sci.* **12** e2024EA003725

[76] Baskaran L, Elder C, Bloom A A, Ma S, Thompson D and Miller C E 2022 Geomorphological patterns of remotely sensed methane hot spots in the Mackenzie Delta, Canada *Environ. Res. Lett.* **17** 015009